J. Mat. NanoSci. 2021, 8(1), 16-22 Article

Journal of
Materials NanoScience

X-ray and Raman study of $CH_3NH_3PbI_3$ perovskite nanocrystals

B. Gopal Krishna,[1*] Dhriti Sundar Ghosh,[2] Sanjay Tiwari,[1]

[1]Photonics Research Laboratory, School of Studies in Electronics & Photonics, Pt. Ravishankar Shukla University, Raipur, 492010, India. [2]Department of Physics, Indian Institute of Technology, Bhilai, 492015, India.

Submitted on: 04-July-2021 Accepted and Published on: 30-July-2021

ABSTRACT

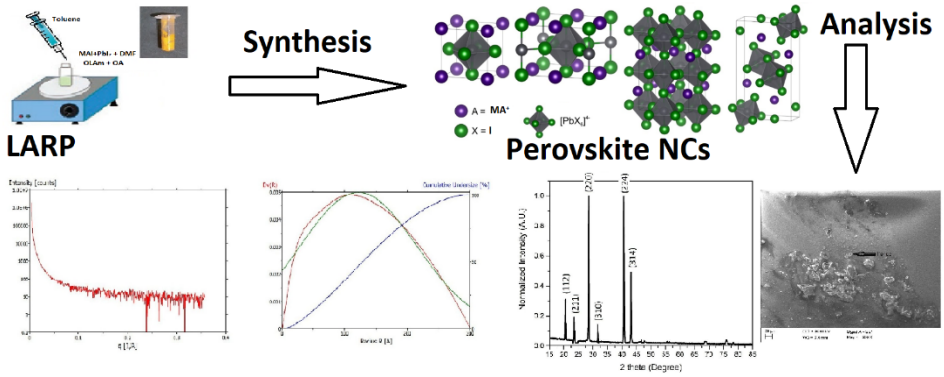

Organic-inorganic hybrid perovskite nanocrystals have gained considerable attention for optoelectronics applications due to their unique properties like high light absorption coefficient, band gap tunability, and larger diffusion length. In this work, the ligand-assisted re-precipitation method (LARP) was employed to synthesize $CH_3NH_3PbI_3$ nanocrystals (NCs). The optical and structural properties of nanocrystals depend on their size. X-ray diffraction (XRD) and small-angle X-ray scattering (SAXS) techniques are used to determine the crystal structure, particle size distribution, and surface to volume ratio of $CH_3NH_3PbI_3$ nanocrystals. The organic-inorganic interactions of $CH_3NH_3PbI_3$ nanocrystals are studied by Raman spectra at room temperature. This study will provide the basis to interpret the morphological properties of perovskite nanocrystals for their full exploitation in different optoelectronics applications.

Keywords: $CH_3NH_3PbI_3$ nanocrystals, Ligand-assisted re-precipitation method, XRD, SAXS, Raman spectra.

INTRODUCTION

Metal halide perovskites have achieved incredible advances as optoelectronic materials due to extraordinary properties like excellent luminescence properties, high light absorption coefficient, and band gap tunability. The materials are used to fabricate photovoltaic cells, LEDs, and display applications. Perovskite materials have an exceptional combination of optical and electronic properties. The fundamental understanding of perovskite material can lead to developing many technological applications. Halide perovskites have the formula ABX_3 in which 'A', 'B' and 'X' are monovalent cation (MA or FA or Cs), divalent cation (Pb or Sn), and halides (I or Cl or Br) anions respectively.[1–3] In the perovskite crystal structure, 'B' is coordinated with six 'X' ions to form an octahedral structure. 'A' cation is positioned in between the octahedral structure. Perovskite can be all-inorganic or organic-inorganic material that depends upon the 'A' cation. The optical and structural properties of this material depend upon its composition.[4] The dimensions of perovskite material can be 0D or 2D or quasi-2D or 3D structure.[5,6] The crystal structure of a perovskite material can be known by tolerance factor 't' and an octahedral factor 'u'. The tolerance factor is given by equation as

$$t = \frac{r_A + r_B}{\sqrt{2}(r_B + r_X)} \quad (1)$$

*Corresponding Author: B Gopal Krishna , Photonics Research Laboratory, School of Studies in Electronics & Photonics, Pt. Ravishankar Shukla University, Raipur,492010, India
Address: Pt. Ravishankar Shukla University, Raipur,492010, India
Tel: xx
Email: krishna_burra85@yahoo.com

Cite as: *J. Mater. NanoSci., 2021, 8(1), 16-22.*

 ISSN 2394-0867 http://pubs.iscience.in/jmns

where, r_A, r_B and r_X are the ionic radii of A, B, and X atoms respectively. The octahedral factor 'u' is also an important parameter to predict the crystal structure of perovskite and given by

$$u = \frac{r_B}{r_X} \quad (2)$$

The values of tolerance factor and octahedral factor are 0.813< t <1.107 and 0.442< u <0.895 respectively which gives the information of probable formation of ABX_3 perovskite structure[6]. The properties of perovskite can be influenced by structural distortions and the type of ions at 'A' or 'B' or 'X' site. The lowering of the dimensional structure of perovskite can be done through compositional and structural engineering. The change in structure and composition in lower-dimensional perovskites can tune the properties like bandgaps, binding energies, and transport properties of the material.[7]

In this work, the study of $CH_3NH_3PbI_3$ nanocrystal structure is done by using a technique that does not destroy the sample. X-ray diffraction (XRD) and small-angle X-ray scattering (SAXS) are non-destructive methods that are used to find out the structure, the surface to volume ratio, and spatial size of $CH_3NH_3PbI_3$ nanocrystals. The size of the crystals under investigation should have a magnitude from nanometers to hundreds of nanometers. SAXS is the unique measurement tool for determining the phase dimensions in material, size and shape of nanocrystals, and particle size distribution.[8,9] SAXS curve is expressed as a power function at the small angle peak slope as per Porod's law. The magnitude of the power is associated with the fractal dimension of the structure of the crystal demonstrating atomic matrix geometry. The magnitude of power for a low dimensional matrix is near to the dimension itself and four for 3D dense dispersed media. The interplanar distances in the layered or superlattice crystal are to be characterized as Bragg peaks at the SAXS curve for which the positions will obey Bragg's law. In X-ray scattering, Guinier's law provides the approximation initial portion of scattering intensity through exponential function. Porod's law provides the approximation of the intensity curve of large scattering angles. The position, orientation, and rotation around the C-N bond of the MA^+ cation within the perovskite network cannot be determined completely by using X-ray diffraction studies. Therefore, organic-inorganic interactions of $CH_3NH_3PbI_3$ nanocrystals are studied by Raman spectra at room temperature. There are dynamically disordered states in MA^+ cations due to the orientation and rotation around the C-N bond of the MA^+ cation.[10–17] The dynamics of MA^+ cations also depend upon the electrostatic interaction between positive MA^+ cations and PbI_3^- framework. The electrostatic interaction in the perovskite is governed by the hydrogen bond interactions between NH_3^+ ion and halide ions in the $MAPbI_3$ material. The transition between Pb(6s)–I(5p) valence bands and Pb(6p) conduction bands is responsible for the origination of the optical band gap. MA^+ cation and PbI_3^- network interactions also influence the exciton binding energy, charge carrier lifetime, and photoluminescence properties of the $MAPbI_3$ perovskite.[15,16,18–20] Therefore, Raman spectroscopy is a technique to study the phase transitions, lattice dynamics, and interactions between the organic and inorganic molecules of $MAPbI_3$ perovskite. Raman spectroscopy can be used to detect low-wavenumber lattice vibrations in perovskites. There is a possibility of damage of $MAPbI_3$ perovskite under strong laser irradiation during Raman spectroscopy. The vibrational relaxation, phase transition, and organic cation and the PbX_3^- network interactions in $MAPbI_3$ perovskite can be studied by analyzing Raman spectra. The rotational dynamics of MA^+ cations can be investigated by this spectrum which is closely related to the optical properties of $MAPbI_3$ perovskite. Therefore, a vibrational spectroscopy study of $MAPbI_3$ can be done by using Raman spectroscopy.[21–25]

RESULTS AND DISCUSSION

X-ray diffraction and small-angle X-ray scattering analysis of $CH_3NH_3PbI_3$ Nanocrystals

XRD pattern and SEM of the $CH_3NH_3PbI_3$ NCs and nanocrystal thin film are shown in Figure 1 (a) and (b) respectively. The sample is in a single phase with no secondary phase detection as per the XRD pattern. The diffraction pattern shows that the sample is indexed with a Pm3m (Z=1) space group cubic crystal structure. The intensive peaks corresponding to $CH_3NH_3PbI_3$ nanocrystal lattice reflections of Cu Kα photons were found to be 2θ/deg: 20.5˚, 23.4˚, 28.5˚, 31.6˚, 40.6˚ and 43.1˚ with crystallographic planes (112), (211), (220), (310), (224), and (314) respectively. $CH_3NH_3PbI_3$ nanocrystal particle size is calculated by Scherrer model which is found out to be 30 nm. SAXS measurements show that particle size is ranging between 20-40 nm.

Initially, the structure of $CH_3NH_3PbI_3$ nanocrystals is analyzed in the form of film to know the average size of the particles. The X-ray beam is transmitted through $CH_3NH_3PbI_3$ NC thin film along the surface normal to it. The intensity distribution of the beam is recorded with the help of an area detector by blocking the direct beam. The intensity of the SAXS is symmetric around the position of the transmitted beam which represents the isotropic nature of particles in the film within the plane of the sample surface. The azimuthally SAXS signal I(q) versus the scattering vector q is depicted in Figures 2 (a) and 3(a) for nanocrystal film and nanocrystal powder respectively. Therefore, SAXS intensity I(q) can be interpreted as the product of structure factor S(q) and $F^2(q)$ which gives the information about the particle size. The size of the particles in the thin film can be evaluated by the squared form factor $F^2(q)$ which is described in equation 6.[9,26]

SAXS intensity $I(q)=F^2(q)S(q)$ (4)

Scattering vector $q = \frac{4\pi}{\lambda}\sin(\frac{\theta}{2})$ (5)

Here θ is scattering angle, λ is x-ray wavelength

Squared form factor

$$F^2(q) = constant.\, q^{-1}.\sum_r p(r).\left[r.\frac{J_1(q.\sin(\alpha).r)}{q.\sin(\alpha)}\right]^2.e^{-\sigma p^2 q^2} \quad (6)$$

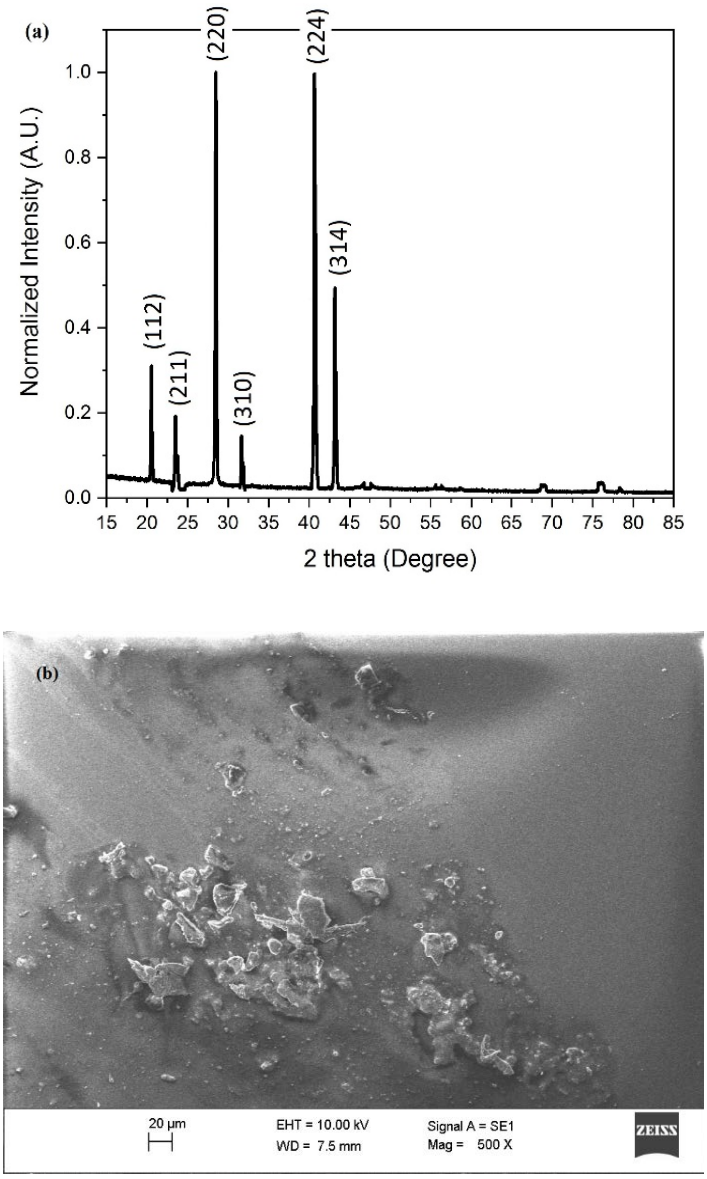

Figure 1 a) XRD pattern of $CH_3NH_3PbI_3$ nanocrystals and (b) SEM image of $CH_3NH_3PbI_3$ nanocrystals thin film

The factor q^{-1} and particle radius are due to the finite angle dispersion of the particle axes, and discrete sum averaging using a Gaussian particle radius distribution function p(r). The angle between particle axis, scattering vector, and Bessel function of the first order is represented by a, q, and J_1 respectively.[26] Thus, results obtained from SAXS can determine the particle size present in the $CH_3NH_3PbI_3$ thin film which will help to optimize the parameters for fabricating good thin films. The size distribution function $D_v(R)$ versus the particle size parameter R is depicted for $CH_3NH_3PbI_3$ NC thin film and nanocrystal powder in Figures 2 (b) and 3(b) respectively. The results suggest that particles are oriented along their axes along the surface normal of the films according to Figure 2. The data is corrected by taking the SAXS of the empty sample holder before doing SAXS of $CH_3NH_3PbI_3$ NCs.

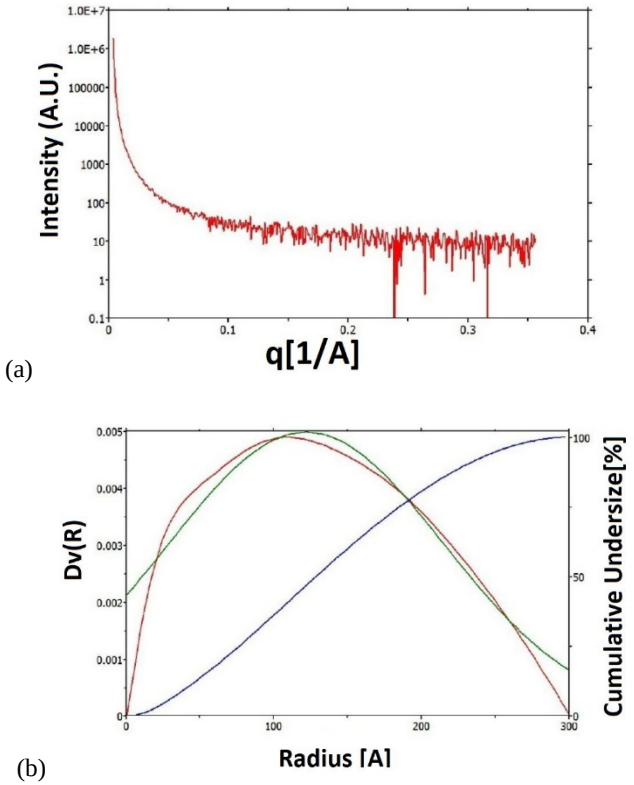

Figure 2 SAXS pattern for $CH_3NH_3PbI_3$ nanocrystal thin film

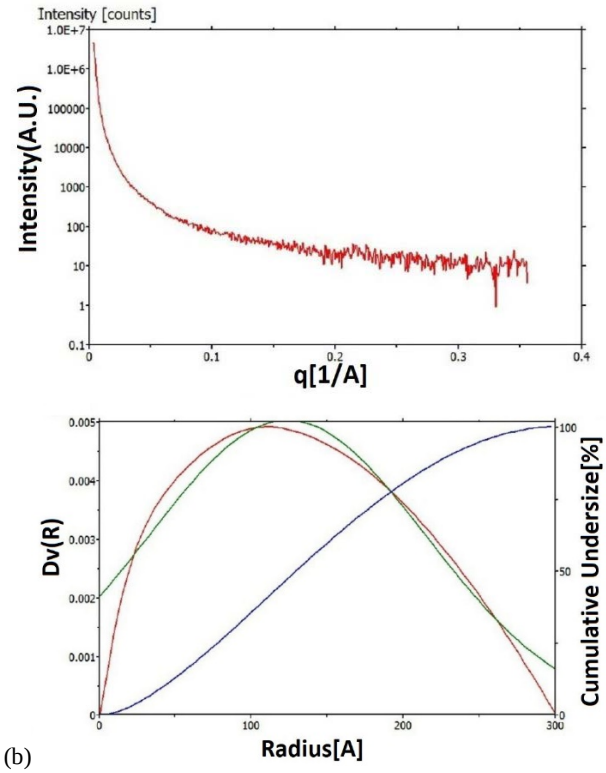

Figure 3. SAXS pattern for $CH_3NH_3PbI_3$ nanocrystal powder

The SAXS data analysis shows that the average spatial size and surface-to-volume ratio (S/V) of particles in $CH_3NH_3PbI_3$ NC thin

film are up to 26 nm and 0.0387 $Å^{-1}$ as shown in Figures 2(a) and (b). The average spatial size and surface-to-volume ratio (S/V) of $CH_3NH_3PbI_3$ NCs powder are up to 26 nm and 0.0377 $Å^{-1}$ as shown in Figure 3(a) and (b). SAXS data of both $CH_3NH_3PbI_3$ NC thin film and $CH_3NH_3PbI_3$ nanocrystal powder is nearly the same. Therefore, the particle size of nanocrystals can be predicted by SAXS both in thin film or powder form accurately. The wavelength of λ = 1.54 $Å$ is used to perform SAXS on the sample to obtain the scattering vector q ranging between 0 < q < 0 .4. Other dimensional structural components are also detected within the $CH_3NH_3PbI_3$ NC thin film sample because the curve of SAXS is uneven between 0.2 to 0.4 $Å^{-1}$.[9,26–28] The values obtained from the graphical analysis of parameters by the SAXS technique are showed in Table 1.

Table 1. The particle size of perovskite nanocrystals obtained from the SAXS technique

Approximation Method	Parameters	$CH_3NH_3PbI_3$ NCs	$CH_3NH_3PbI_3$ NC thin film
Graphical Approximation	**Most frequent radius**	11.10nm	10.80nm
	Average radius	13.3nm	13.21nm
	R20	6.66nm	6.51nm
	R50	12.92nm	12.82nm
	R80	19.84nm	19.78nm
	Surface to Volume ratio (S/V)	0.0377 1/A	0.0387 1/A
	Relative standard deviation	51.64 %	52.29 %
By Gaussian approximation	**R20**	6.26nm	6.08nm
	R50	12.33nm	12.14nm
	R80	18.39nm	18.19nm
	Surface to Volume ratio (S/V)	0.0456 1/A	0.0465 1/A
	Relative standard deviation	74.08 %	76.64 %

Here, the parameters R20, R50, and R80 represent cumulative undersize of 20%, 50%, and 80% respectively.

The particle size distribution of $CH_3NH_3PbI_3$ NCs from SAXS data is statistically average than XRD analysis. SAXS is responsive to the size of the fluctuation region of electronic density. XRD is responsive to the size of the long-range order region.[26] Guinier's law is applicable to know the particle size of the $CH_3NH_3PbI_3$ NCs sample by the SAXS experiment. Particle size distribution of $CH_3NH_3PbI_3$ NCs sample is analyzed by parametric distribution model method. In this model method, all nanocrystals have different sizes within the same shape. For a size of nanocrystal 'R', the particle size distribution $D_V(R)$ is assumed to know the size parameter of the nanocrystal system. The scattering intensity for the nanocrystal system is given by the equation.

$$I(s) = \int_0^\infty i_0\,(sR) D_V(R) m^2(R) dR \qquad (7)$$

Here, s is the scattering vector, $i_0(sR)$ is a form factor for a particle of size R, m(R) is the volume of a particle having size parameter R and $D_v(R)$ is size distribution function. The mean and standard deviation parameters in the normal distribution are determined by the size distribution function. Scattering intensity 'I(s)' depends on these parameters. A general optimization algorithm of the model relates the theoretical and experimental scattering intensity to find out the particle size distribution. Scattering intensity 'I(s)' is approximated by Guinier's law with the help of Gaussian distribution to find out the particle size distribution of the sample.[21,26]

Raman spectra

The Raman spectrum of $CH_3NH_3PbI_3$ was conducted by a Raman spectrometer. The narrow band laser is used as the light source to avoid fluorescence interference from perovskite. The Raman spectra of $MAPbI_3$ thin film at room temperature (300 K) with 830 nm excitation are shown in Figure 4. Raman bands in $MAPbI_3$ nanocrystal thin film are appeared at 909 cm^{-1}, 958 cm^{-1},1252 cm^{-1}, 1424 cm^{-1}, 1472 cm^{-1} and 1580 cm^{-1} respectively. The appearance of these bands suggests that there is a strong interaction between MA^+ cation and inorganic PbI_3^- framework in the $MAPbI_3$ perovskite. These interactions are due to electrostatic attractions, chemical interactions. The rotation of the MA^+ cation is fast at room temperature. The embedded MA^+ cation in $MAPbI_3$ perovskite experiences an unequal environment during rotation. This unequal environment during rotation breaks the average crystal symmetry of the PbI_3^- network due to which rotation mode becomes Raman active under a restricted condition. Chen et al. reported the tetragonal phase MA^+ in the cage of the PbI_3^- network exhibited four-fold rotational symmetry of the C-N axis

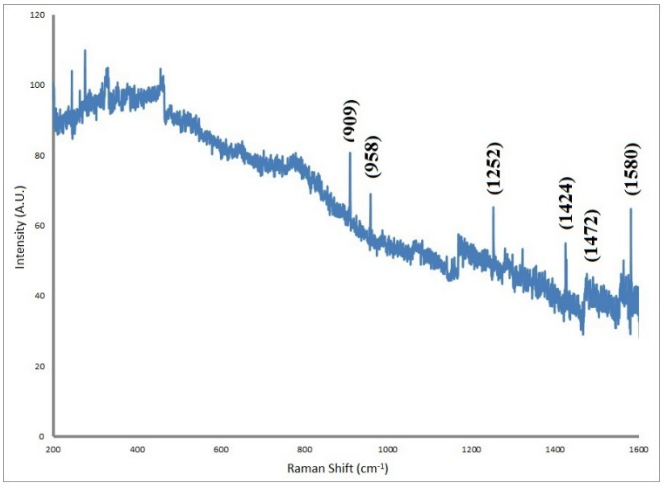

Figure 4 The evolution of Raman spectra of $MAPbI_3$ under 26 mW 407 nm laser with measurements were conducted at ambient conditions.

(C4 mode) and three-fold rotation around the C-N axis (C3 mode) at room temperature.[27,28] Brivio et al. reported the rotation mode of MA^+ cation against NH_3^+ ion in the tetragonal $MAPbI_3$ perovskite was around 300 cm^{-1} at room temperature. These predictions were concluded by using first-principles lattice dynamics.[29]

The restricted rotation of the MA^+ ion in $MAPbI_3$ thin films is around 275 cm^{-1} as shown in Figure 4. The characteristic Raman band at 275 cm^{-1} for rotation mode of MA^+ cation against NH_3^+ ion around the C-N axis is the C3 mode. Raman bands for $MAPbI_3$ perovskite below 200 cm^{-1} and above 400 cm^{-1} are due to lattice vibrations and intramolecular vibrations of MA^+ ion respectively. The observed Raman band assigned to the MA^+ cage vibration at 240-249 cm^{-1} is abnormal which has originated from the thermally induced weakening of the H--I interactions. Raman band at 909 cm^{-1} corresponds to MA^+ rocking mode. Raman band at 958 cm^{-1} corresponds to C-N stretching mode. Raman band at 1424 cm^{-1} corresponds to NH_3^+ symmetric bending. Raman band at 1580 cm^{-1} corresponds to NH_3^+ twisting mode. The sharp and intense band at 958 cm^{-1} and 1462 cm^{-1} corresponds to C-N stretching and NH_3^+ asymmetric bending respectively which indicates a strong interaction from the inorganic framework. The observed rocking mode at 1252 cm^{-1} and the twisting mode (NH_3^+) at 1580 cm^{-1} in $MAPbI_3$ perovskite indicates that the sensitivity of vibrational modes of the MA^+ cation towards microenvironment.[24] Halides play an important role in the variation of the microenvironment of PbI_3^- network. The bands correspond to NH_3^+ is more sensitive to the microenvironment of the inorganic component of $MAPbI_3$ perovskite due to hydrogen bonding of N^+-H…X. There is a strong hydrogen bonding in $MAPbI_3$ perovskite at room temperature. The C-N stretching mode of MA^+ ions indicates the reduction of the lattice constant of the perovskite. There is an influence of the size of MA^+ ions on the restricted rotation which impacts the activation energy of C4 mode. The increase in the size of MA^+ ions increases the activation energy of C4 mode. C3 mode is less influenced by the size of MA^+ ions due to which the band frequency remains almost unaffected[30–35]. Hydrogen bonding between NH_3^+ ion and the halides in the $MAPbI_3$ perovskite structure (N^+-H…X) has an important role in the rotational dynamics of the organic cation along the C–N axis. Cation–anion electrostatic attraction and hydrogen bonding play an important role in organic–inorganic chemical interaction in perovskite. This is the reason that the variation of the perovskite composition is done to tune their energy band gap to get highly efficient solar cells. The use of a larger cation at 'A' site or replacing halides at 'X'- site in ABX_3 structure will change the overall organic-inorganic interaction to obtain highly stable perovskite materials for optoelectronic applications. There is no direct contribution of MA^+ cation in $MAPbI_3$ perovskite to the formation of the valence and conduction band structure. The dipole created in the octahedral framework attribute to dielectricity, ferroelectricity, and antiferroelectricity properties.[36–38] The behavior of the cations in the inorganic framework is strongly dependent on the microenvironment of MA^+ cation and PbI_3^- octahedral framework interactions. The rotation of MA^+ cation can lower the exciton binding energy which helps charge carrier separation and transportation in perovskites. The optimization of the chemical structure and geometry of the MA^+ cation and inorganic-organic interactions in $MAPbI_3$ will improve the performance of optoelectronic devices. Raman spectral bands will help in identifying the chemical composition of the perovskite.[39–43]

EXPERIMENT

Ligand-assisted re-precipitation method (LARP) was employed to synthesize $CH_3NH_3PbI_3$ nanocrystals (NCs) as shown in Figure 5. $CH_3NH_3PbI_3$ precursor solution was prepared by dissolving 1millimoles (mmol) methylammonium iodide (MAI) and 1 millimoles (mmol) lead iodide (PbI_2) into 1 ml dimethylformamide (DMF) solvent in a 100 ml round bottom flask under N_2 environment with continuous stirring at 500 rpm at room temperature for 3 hours. 0.5 ml oleylamine (OLAm) and 0.5 ml oleic acid (OA) were mixed in a separate 100 ml two-necked round bottom flask and stirred continuously at 500 rpm at room temperature for 3 hours. 1 ml $CH_3NH_3PbI_3$ precursor solution was injected into the OLAM+OA mixture and stirred continuously at 500 rpm at room temperature for 1 hour. Then, 5 ml toluene was injected into the obtained precursor solution with continuous stirring at 400 rpm for 2 hours. The solution was centrifuged at 6000 rpm for 20 minutes. The supernatant was removed and obtained nanocrystal precipitate was washed by toluene 3 to 4 times. After washing the nanocrystal precipitate, green- colored $CH_3NH_3PbI_3$ NCs were obtained. The oleylamine acted as an inhibitor to slow down the crystallization rate of $CH_3NH_3PbI_3$ NCs in the LARP process.[28]

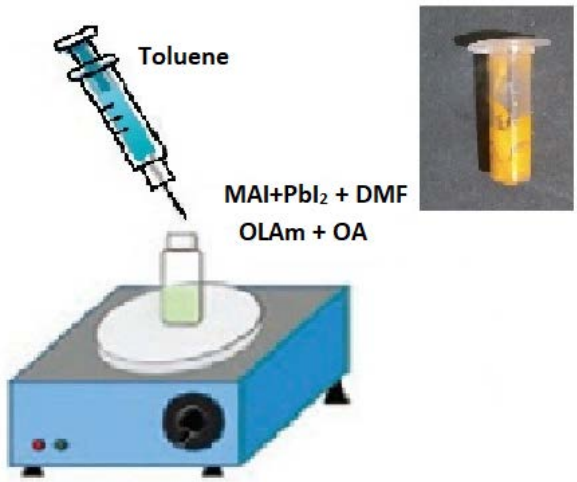

Figure 5. Schematic illustration of LARP method to prepare $CH_3NH_3PbI_3$ nanocrystals

CONCLUSIONS

In this work, $CH_3NH_3PbI_3$ NCs were synthesized by the ligand-assisted re-precipitation method by using oleylamine as the inhibitor. The rate of crystallization of $CH_3NH_3PbI_3$ nanocrystals slows down due to the use of oleyamine which can impact the crystal quality and structure of nanocrystals. The method of

analysis of structure and particle size of $CH_3NH_3PbI_3$ NCs can be selected on the basis of the degree of polydispersity of the sample, particle concentration, and type of particle size distribution. The structure and particle size distribution analyses are carried out by XRD and SAXS techniques. Small-angle X-ray scattering analysis is found to be an effective and non-destructive technique to know the structure, particle size distribution, and surface to volume ratio of $CH_3NH_3PbI_3$ NCs.

Raman spectroscopic measurements will help to study the organic-inorganic interactions of $MAPbI_3$ perovskites. Raman spectrum of $MAPbI_3$ is obtained with a wide range of wavenumbers which includes different modes like restricted rotation modes, and rocking mode of MA^+ ion, C-N stretching mode, NH_3^+ symmetric bending and NH_3^+ twisting mode. The Raman bands of the MA^+ cation in $MAPbI_3$ perovskite indicate the chemical interactions between MA^+ cation and PbI_3^- framework. The restricted rotation mode of the MA^+ cation is identified by C3 mode along the C-N axis. The result shows that the interaction between MA^+ cation and PbI_3^- octahedral framework is because of the hydrogen bonding. Raman spectroscopy enables us to understand the role of cation and halide interactions for tuning the energy bandgap of perovskite. Raman spectroscopic measurements can give fingerprint details about organic-inorganic interactions of perovskites which will be helpful for accurate data analysis and comparisons of perovskite materials. The findings of the present work through X-ray diffraction, SAXS, and Raman spectroscopic measurements are valuable in understanding the role of cations and halides in the performance of $MAPbI_3$ in various optoelectronic applications.

ACKNOWLEDGEMENTS

We gratefully thank the technical support from National Institute of Technology, Raipur, India.

Conflict of Interest: Authors declare no conflict of interest.

REFERENCES AND NOTES

1. H.-S. Kim, C.-R. Lee, J.-H. Im, et al. Lead Iodide Perovskite Sensitized All-Solid-State Submicron Thin Film Mesoscopic Solar Cell with Efficiency Exceeding 9%. *Scientific Reports* **2012**, 2 (1), 1–7.
2. B. Gopal Krishna, S. Tiwari. Modeling of Abnormal Hysteresis in CsPbBr3 based Perovskite Solar Cells. *J. Ravishankar University* **2021**, 34 (1), 01–08.
3. B.G. Krishna, D. Sundar Ghosh, S. Tiwari. Progress in ambient air-processed perovskite solar cells: Insights into processing techniques and stability assessment. *Solar Energy* **2021**, 224, 1369–1395.
4. A. Abrusci, S.D. Stranks, P. Docampo, et al. High-performance perovskite-polymer hybrid solar cells via electronic coupling with fullerene monolayers. *Nano let.* **2013**, 13 (7), 3124–3128.
5. J. Burschka, N. Pellet, S.J. Moon, et al. Sequential deposition as a route to high-performance perovskite-sensitized solar cells. *Nature* **2013**, 499 (7458), 316–319.
6. L. N. Quan, B. P. Rand, R. H. Friend, et al. Perovskites for Next-Generation Optical Sources. *Chemical reviews* **2019**, 119 (12), 7444–7477.
7. B. Li, Y. Kawakita, Y. Liu, et al. Polar rotor scattering as atomic-level origin of low mobility and thermal conductivity of perovskite CH $_3$ NH $_3$ PbI $_3$. *Nature Communications 2017 8:1* **2017**, 8 (1), 1–9.
8. S. Joshi, Z.I. Hasan, M. Pruthvi, M.P. Tulsiram. X-ray diffraction – A simplistic approach for perovskite based solar cells degradation studies. *Materials Today: Proceedings* **2021**, 35, 31–34.
9. J.M. Roemer, S. Demchyshyn, A. Böhm, et al. X-ray study of anisotropically shaped metal halide perovskite nanoparticles in tubular pores. *Applied Physics Letters* **2018**, 113 (25), 251901.
10. N. Onoda-Yamamuro, T. Matsuo, H. Suga. Calorimetric and IR spectroscopic studies of phase transitions in methylammonium trihalogenoplumbates (II)†. *Journal of Physics and Chemistry of Solids* **1990**, 51 (12), 1383–1395.
11. K. Yamada, S. Hino, S. Hirose, et al. Static and Dynamic Structures of Perovskite Halides ABX_3 (B = Pb, Sn) and Their Characteristic Semiconducting Properties by a Hückel Analytical Calculation. **2018**, 91 (8), 1196–1204.
12. A.M.A. Leguy, J.M. Frost, A.P. McMahon, et al. The dynamics of methylammonium ions in hybrid organic-inorganic perovskite solar cells. *Nature communications* **2015**, 6.
13. E. Mosconi, C. Quarti, T. Ivanovska, G. Ruani, F. De Angelis. Structural and electronic properties of organo-halide lead perovskites: a combined IR-spectroscopy and ab initio molecular dynamics investigation. *Physical chemistry chemical physics* **2014**, 16 (30), 16137–16144.
14. M.T. Weller, O.J. Weber, P.F. Henry, A.M. di Pumpo, T.C. Hansen. Complete structure and cation orientation in the perovskite photovoltaic methylammonium lead iodide between 100 and 352 K. *Chem. Commun.* **2015**, 51 (20), 4180–4183.
15. T. Umebayashi, K. Asai, T. Kondo, A. Nakao. Electronic structures of lead iodide based low-dimensional crystals. *Physical Review B* **2003**, 67 (15), 155405.
16. E. Mosconi, A. Amat, Md.K. Nazeeruddin, M. Grätzel, F. de Angelis. First-Principles Modeling of Mixed Halide Organometal Perovskites for Photovoltaic Applications. *J. Physical Chem. C* **2013**, 117 (27), 13902–13913.
17. B.G. Krishna, S. Tiwari. Optical properties of $CsPbBr_3$ perovskite nanocrystals with silver nanoparticles using a room-temperature synthesis process. *Optical Materials* **2021**, 119, 111357.
18. G. Grancini, S. Marras, M. Prato, et al. The Impact of the Crystallization Processes on the Structural and Optical Properties of Hybrid Perovskite Films for Photovoltaics. *Journal of Physical Chemistry Letters* **2014**, 5 (21), 3836–3842.
19. A. Filippetti, A. Mattoni. Hybrid perovskites for photovoltaics: Insights from first principles. *Physical Review B* **2014**, 89 (12), 125203.
20. B. Gopal Krishna, G.S. Rathore, N. Shukla, S. Tiwari. Perovskite solar cells: A review of architecture, processing methods, and future prospects. *Hybrid Perovskite Composite Materials* **2021**, 375–412.
21. J.-S. Park, S. Choi, Y. Yan, et al. Electronic Structure and Optical Properties of α-CH 3 NH 3 PbBr 3 Perovskite Single Crystal. *J. Phys. Chem. Lett* **2015**, 6, 4308.
22. C. Wehrenfennig , M. Liu, H.J. Snaith, M.B. Johnston, L.M. Herz. Homogeneous Emission Line Broadening in the Organo Lead Halide Perovskite $CH_3NH_3PbI_{3-x}Cl_x$. *J. physical chem. Lett.* **2014**, 5 (8), 1300–1306.
23. P. Delugas, A. Filippetti, A. Mattoni. Methylammonium fragmentation in amines as source of localized trap levels and the healing role of Cl in hybrid lead-iodide perovskites. *Physical Review B* **2015**, 92 (4), 045301.
24. J. Liu, O.V. Prezhdo. Chlorine doping reduces electron-hole recombination in lead iodide perovskites: time-domain ab initio analysis. *J. physical chem. Lett.* **2015**, 6 (22), 4463–4469.
25. T. Kirchartz, T. Markvart, U. Rau, D.A. Egger. Impact of Small Phonon Energies on the Charge-Carrier Lifetimes in Metal-

Halide Perovskites. *J. Physical Chem. Lett.* **2018**, 9 (5), 939–946.
26. M.D. Sharkov, M.E. Boiko, S.N. Ivashevskaya, N.S. Belyakova. Studying Ultradisperse Diamond Structure within Explosively Synthesized Samples via X-Ray Techniques. *J. Physics* 11.
27. T. Chen, B.J. Foley, B. Ipek, et al. Rotational dynamics of organic cations in the $CH_3NH_3PbI_3$ perovskite. *Physical chemistry chemical physics* **2015**, 17 (46), 31278–31286.
28. X. He, C. Jian, W. Hong, Q. Cai, W. Liu. Ultralong $CH_3NH_3PbI_3$ nanowires synthesized by a ligand-assisted reprecipitation strategy for high-performance photodetectors. *J. Mater. Chem. C* **2020**, 8 (22), 7378–7383.
29. F. Brivio, J.M. Frost, J.M. Skelton, et al. Lattice dynamics and vibrational spectra of the orthorhombic, tetragonal, and cubic phases of methylammonium lead iodide. *Physical Review B* **2015**, 92 (14), 144308.
30. D.P. McMeekin, G. Sadoughi, W. Rehman, et al. A mixed-cation lead mixed-halide perovskite absorber for tandem solar cells. *Science (New York, N.Y.)* **2016**, 351 (6269), 151–155.
31. Y. Liu, Z. Yang, D. Cui, et al. Two-Inch-Sized Perovskite $CH_3NH_3PbX_3$ (X = Cl, Br, I) Crystals: Growth and Characterization. *Adv. Mater.* **2015**, 27 (35), 5176–5183.
32. T. Zhang, M. Yang, E.E. Benson, et al. A facile solvothermal growth of single crystal mixed halide perovskite $CH_3NH_3Pb(Br_{1-x}Cl_x)_3$. *Chem. Commun.* **2015**, 51 (37), 7820–7823.
33. N. Meinander, S. Forss, G. Bergström. A Raman spectroscopic study of methyl ammonium chloride: III—The internal vibrations in the 600–1700 cm−1 frequency region. *Journal of Raman Spectroscopy* **1981**, 11 (3), 155–167.
34. Y. Fang, Q. Dong, Y. Shao, Y. Yuan, J. Huang. Highly narrowband perovskite single-crystal photodetectors enabled by surface-charge recombination. *Nature Photonics 2015 9:10* **2015**, 9 (10), 679–686.
35. D.B. Mitzi. Synthesis, Crystal Structure, and Optical and Thermal Properties of $(C_4H_9NH_3)_2MI_4$ (M = Ge, Sn, Pb). *Chem. Mater.* **1996**, 8 (3), 791–800.
36. S. Meloni, G. Palermo, N. Ashari-Astani, M. Grätzel, U. Rothlisberger. Valence and conduction band tuning in halide perovskites for solar cell applications. *J. Mater. Chem. A* **2016**, 4 (41), 15997–16002.
37. J. Shi, X. Xu, H. Zhang, et al. Intrinsic slow charge response in the perovskite solar cells: Electron and ion transport. *Applied Physics Lett* **2015**, 107 (16), 163901.
38. X. Zheng, B. Chen, C. Wu, S. Priya. Room temperature fabrication of $CH_3NH_3PbBr_3$ by anti-solvent assisted crystallization approach for perovskite solar cells with fast response and small J–V hysteresis. *Nano Energy* **2015**, 17, 269–278.
39. S. Ruan, M.-A. Surmiak, Y. Ruan, et al. Light induced degradation in mixed-halide perovskites. *J. Mater. Chem. C* **2019**, 7 (30), 9326–9334.
40. A.K. Sivadasan, P. Dhara, C. Singha, et al. Role of polarized tip-enhanced Raman spectroscopy in the enhancement of interface optical phonon modes in AlGaN multi-quantum wells *J. Mat. NanoSci* **2020**, 7(1), 19-23.
41. S. Sardar, P. KAR, S.K. Pal. The Impact of Central Metal Ions in Porphyrin Functionalized ZnO/TiO_2 for Enhanced Solar Energy Conversion wells. *J. Mat. NanoSci* **2014**, 1(1), 12-30.
42. A.K. Pollard, N. Kumar, A. Rae, et al. Nanoscale Optical Spectroscopy: An Emerging Tool for the Characterisation of 2 D Materials. wells *J. Mat. NanoSci* **2014**, 1(1), 39-49.
43. T.V.B. Nagaveni, K.M. Mahadevan, R. Naik, T.O.S. Kumara. Synthesis of blue light emitting 5-carboxylicacid-2-arylsubstituted benzimidazoles as photosensitizers for dye-sensitized solar cells. wells *J. Mat. NanoSci* **2020**, 7(1), 24-28